

Direct Simulation Monte Carlo of Inductively Coupled Plasma and Comparison with Experiments

Justine Johannes,* Timothy Bartel, Gregory A. Hebner, and Joseph Woodworth

Sandia National Laboratories, Albuquerque, New Mexico 87185-0826, USA

Demetre J. Economou*

Plasma Processing Laboratory, Department of Chemical Engineering, University of Houston, Houston, Texas 77204-4792, USA

ABSTRACT

Direct simulation Monte Carlo was used to study ion and neutral transport and reaction in a low-gas-pressure high-plasma-density inductively coupled reactor with chlorine (electronegative) chemistry. Electron density and temperature were computed by a self-consistent continuum plasma code and were used as input to the direct simulation Monte Carlo code. Simulation results were compared with experimental data taken in a Gaseous Electronics Conference reference cell modified for inductive plasma operation. Data on the radial distribution of positive ion density (Cl^+), negative ion density (Cl^-), as well as the energy distribution of ions bombarding the substrate electrode compared favorably with simulation results. In addition, the measured atomic chlorine density variations with pressure and power were captured by the simulation.

Introduction

As microelectronic device linewidths continue to shrink below $0.35\ \mu\text{m}$, and aspect ratios continue to increase, the requirements for uniform, selective, and anisotropic etching become ever more stringent. High density plasmas (charge densities $> 10^{17}\ \text{m}^{-3}$) operating at low gas pressure ($< 20\ \text{mTorr}$) can satisfy these requirements.^{1,2} The objective is to deliver a uniform flux of ions and neutrals to the wafer with a controlled ion velocity perpendicular to the surface to achieve directional etching. The species uniformity and the ion angular and energy distribution functions at the wafer (which dictate the shape evolution of microscopic features), depend on reactor design and process conditions, such as gas pressure, power, and frequency.

The strong interdependence of reactor design, operating conditions, and plasma chemistry poses a great challenge in trying to predict the behavior of a plasma reactor based on intuition alone. Mathematical models, tested with experimental data taken under controlled conditions, can assist in the scale-up and optimization of existing processes, and in the development of new reactor designs. Rapid advances in computational power and simulation methodologies have made feasible the self-consistent simulation of multidimensional plasma reactors with complex geometries and chemistries. In fact, a wide range of high density plasma (HDP) reactor simulations have been reported; from zero-dimensional (well-mixed) simulations for chemical mechanism development, to two- and three-dimensional self-consistent simulations.³⁻⁸ However, as the reactor operating pressure decreases, the modeling approach needs to be considered. Theoretically, continuum (fluid) approximations of the transport equations begin to break-down when the molecular mean-free-path becomes comparable to a characteristic length scale of the flow. Physically, the linear transport relationships for mass diffusion, viscosity, and thermal conductivity are no longer valid when the distance molecules travel between collisions is comparable to length scales of interest. This happens when the local Knudsen number $\text{Kn} = \lambda/L > 0.1$, where λ is the mean-free-path of the plasma species and L is a characteristic length scale of the reactor. A typical value of λ for molecules at $10\ \text{mTorr}$ and $500\ \text{K}$ is $0.01\ \text{m}$. Thus, if the characteristic dimension in the flow is less than $0.01\ \text{m}$, fluid approximations must be scrutinized. However, it should be noted that fluid models have been found to perform well even under conditions for which they are expected to break down.⁹

A method appropriate for predicting transitional ($0.1 < \text{Kn} < 1$) and free molecular ($\text{Kn} > 1$) flows is direct simulation Monte Carlo (DSMC), a particle simulation technique.¹⁰ In the past, DSMC has been employed extensively to simulate rarefied gas flows in aerodynamics.^{11,12} Recently, DSMC has been used to simulate low pressure reactors specific to microelectronic device fabrication.¹³⁻¹⁹

In this paper, DSMC is used to describe heavy particle (neutrals and ions) transport in a low pressure inductively coupled plasma reactor. Electrons are not followed by DSMC due to the disparate time scales of electron and heavy particle transport. Rather, a continuum self-consistent plasma simulation is used to obtain two-dimensional (2-D) profiles of the electron temperature (T_e), electron number density (n_e), and time-averaged electrostatic fields (E_r and E_z). These quantities are interpolated onto the DSMC grid to compute electron impact reaction rates and the drift contribution to the ion transport. In this respect, the simulations presented herein can be considered as a particle-fluid hybrid. By using this hybrid, emphasis is placed on the heavy particle transport since it is these particles that affect surface chemistry on the wafer surface. Comparison of simulation results to chlorine plasma data is presented to evaluate the ability of the DSMC-fluid hybrid approach to predict low pressure, electronegative plasma generation, and transport in HDP reactors. The data are taken in a Gaseous Electronic Conference (GEC) reference cell in the range of 20 to 50 mTorr pressure and 185 to 300 W power. Several nonintrusive diagnostics are applied to measure the radial profiles of n_e , T_e , Cl^- , Cl^+ , and ion energy/angular distribution functions. While gas phase and surface chemical mechanisms are still complex, a chlorine plasma provides a "cleaner" electronegative gas system which, at the same time, is practically important. Similar DSMC-fluid hybrid simulations have been reported previously.¹⁹ However, experimental data did not exist for code validation at that time.

Description of Computational Methods

Fluid simulation.—Electron-related quantities and electrostatic fields used in DSMC are from a two-dimensional self-consistent finite element fluid plasma simulation.^{20,21} The corresponding simulation package is named Modular Plasma Reactor Simulator or MPRES.²¹ The power deposited into the plasma, as calculated by a Maxwell equation solver,²² is used as input in an electron energy module to determine the electron temperature and the rate coefficients of electron impact reactions. In turn, these are used as source terms in two separate modules describing ionic and neutral species transport, respectively. The solu-

* Electrochemical Society Active Member.

tion is obtained by iterating among the modules. This modular approach effectively separates the disparate time scales of electron energy, ion transport, and neutral transport. In order to separate the disparate length scales of the problem, the thin (100s of microns) plasma sheath is separated from the bulk plasma. The Poisson equation is not solved in the bulk plasma. Instead, the electron density in the bulk is calculated from the electroneutrality constraint. In addition, the electrons are assumed to be in Boltzmann equilibrium; this provides the electrostatic fields to which ions respond. Modeling equations and boundary conditions have been given before.^{9,20,21} The sheath model is that of Riley.²³ This model solves the ion density continuity equation in a collisionless sheath, and a reduced form of the ion momentum balance by introducing a damping potential to which ions respond. Boltzmann electrons are assumed and the Poisson equation is used to calculate the actual potential distribution. The model is designed to capture the ion motion in the sheath for the intermediate frequency regime. Also, the model appears to capture the two extremes: low frequency for which the ions respond to the instantaneous fields, and high frequency for which the ions respond only to the average fields.

DSMC simulation.—DSMC simulates the fluid as a collection of computational particles,¹⁰ unlike continuum methods which describe the fluid as a matrix of partial differential equations. DSMC provides, in essence, a solution to the Boltzmann equation for the velocity distribution function of the particles. In DSMC, the flow domain is divided into a number of cells. It is assumed that particle motion and particle collisions can be decoupled over a defined time step. The time step size should be smaller than a characteristic time, such as the local mean collision time or the time it takes a particle to cross a cell. The cell size should be smaller than a characteristic length scale, such as the local mean-free-path. During the motion phase, molecules move in free flight according to their starting velocity and the forces acting on the molecules, e.g., an electric field force on an ionized species. During this phase, particles are allowed to cross cell boundaries, collide with the walls (and possibly undergo surface chemistry), or exit the flow field. During the collision phase, collision partners are chosen probabilistically from within each cell. The no-time-counter technique was used to determine the collision frequency. The number of pairs of potential collision partners within a cell is equal to $0.5 N \bar{N} F_n (\sigma_{TC})_{\max} \Delta t / V$, where Δt is the time step size, N is the number of computational particles in the cell, \bar{N} is the time- or ensemble-average value of N , F_n is the number of real particles per simulated particle, $(\sigma_{TC})_{\max}$ is the current maximum of the product of the total cross section and relative velocity in the cell, and V is the cell volume. Gas-phase chemistry takes place during the collision phase. Cross sections for neutral-neutral and ion-neutral collisions are calculated using the variable hard sphere model¹⁰; ion-ion collision cross sections are computed using a screened coulomb potential.²⁴ Three-body collisions are not included. This is certainly a valid assumption at the pressures of interest. Time-average or ensemble-average statistics on interesting quantities (particle density, distribution functions, etc.) are gathered for each cell. The absence of partial differential equations makes DSMC a very robust method, albeit computationally intensive.

A potential difficulty in plasma simulation using DSMC is the disparity of densities between neutral and ion species. For typical HDP reactors, ion densities are 100 to 1000 times lower than the dominant neutral density; and it is difficult to gather meaningful statistics for trace species in a computationally efficient manner. A trace species chemistry model has been implemented for this purpose. Trace species are represented by a larger number (a factor of 100 to 1000) of computational particles compared to the more abundant gas-phase species. To compute the correct number of gas-phase collisions and reactions,

the number of pairs to be selected per cell is computed for three separate cases: trace/nontrace interactions, trace/trace interactions, and nontrace/nontrace interactions. Different collision frequencies are also computed for ion-neutral interactions as compared to neutral-neutral interactions due to the disparity in the relative velocities between the two kinds of pairs. Also, time step subcycling is implemented for ion transport because of the disparate velocities between ions and neutrals.

The electron temperature and electron number density as computed by MPRES are interpolated onto the DSMC grid to determine the spatially varying electron impact reaction probabilities. The electrostatic fields, also from the fluid simulation, are used to calculate the force on ionized species. Frank-Condon effects are modeled by adding the excess energy to the product species when postcollision velocities are determined. The DSMC simulation code is called Icarus. Icarus has been ported to a massively parallel computing environment to compensate for the large computational requirements.

The coupling between DSMC and fluid simulations is shown in Fig. 1. Heavy species profiles predicted by MPRES are used as a starting solution for Icarus. Variables from MPRES interpolated onto the DSMC grid remain static during the Icarus simulation. Cycling neutral species densities between Icarus and MPRES was performed; the updated MPRES solution differed by less than 3% from the original values. Cycling ion densities was attempted too, but proved to be unstable due to differences in the ion boundary conditions between the fluid and particle codes. In essence, DSMC does not impose charge neutrality since the electron density is imported from the fluid simulation (the latter does impose charge neutrality) and DSMC only calculates the ion densities. We are now in the process of correcting this deficiency by imposing the charge neutrality constraint within DSMC.

The DSMC grid used to simulate the GEC reactor is shown in Fig. 2. The geometry of the reactor was simplified by not including the outer ports. The concomitant reduction in surface area was compensated for by increas-

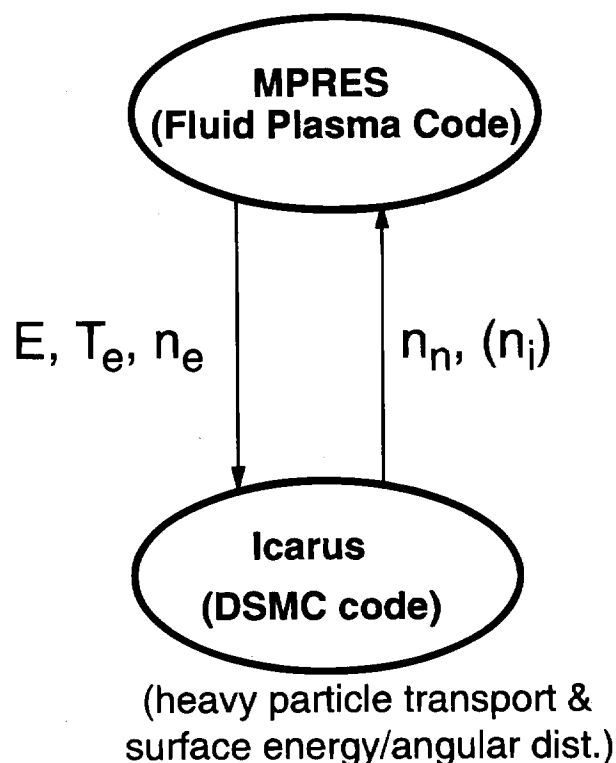


Fig. 1. Schematic of coupling between the continuum plasma code (MPRES) and the DSMC code (Icarus).

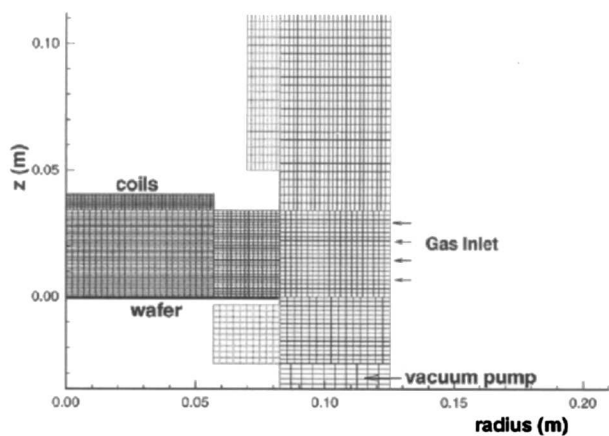


Fig. 2. Two-dimensional DSMC grid used for simulations.

ing the outer wall recombination probability for surface chemistry by a factor of 3.5. The wall temperature was set at 350 K. The gas injection was modeled as a source at the outer radius at the height midway between the upper and lower electrode. Icarus contains a pump module which allows particles to be deleted at a set rate in a zone identified as the pump region. Preliminary neutral flow simulations were performed to determine pumping speeds to be used in the plasma simulations.

The chlorine plasma was modeled using five species: Cl_2 , Cl , Cl^+ , Cl_2^+ , and Cl^- . A list of the gas phase and surface reactions included in the simulations is shown in Table I. A more detailed list including electron-impact excitations, and electron momentum transfer collisions used in the MPRES simulations has been given before.^{5,25} A surface recombination probability of 0.1 was used to describe atomic chlorine recombining to form molecular chlorine. Positive ions were neutralized at the wall and returned as the corresponding neutral with 100% thermal accommodation. Cl^- was reflected at the reactor walls, since negative ions are repelled away from the walls by the electric fields.

Simulations used approximately 5×10^5 computational particles in a grid with 3610 computational cells. The trace species multiplier was 200. Typical simulations run for 5 to 7×10^5 time steps using a time step zone of 1×10^{-6} s and 0.33×10^{-6} s for neutrals and ions, respectively. Typical Icarus simulation times were 8 to 12 h on 512 nodes of an nCUBE-2 massively parallel supercomputer, when started from MPRES solution. MPRES simulations required approximately 0.5 to 3 h on an HP 735-125 workstation.

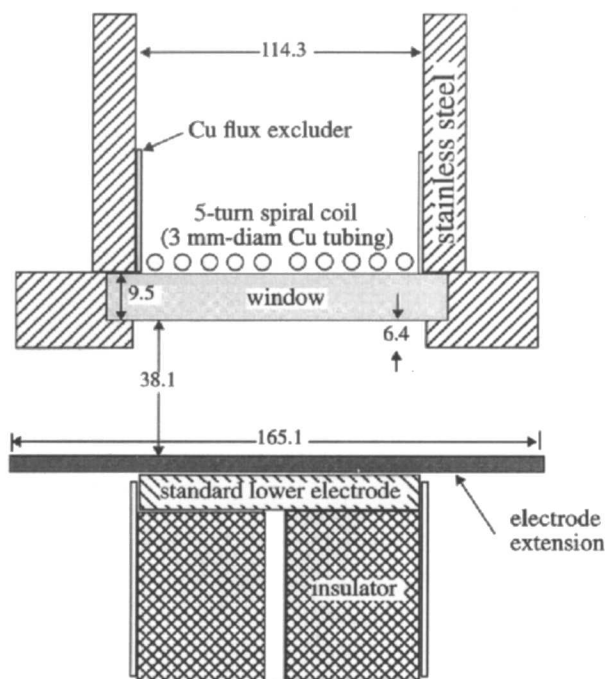


Fig. 3. Gaseous Electronics Conference reference cell configuration with an inductively coupled plasma source. Dimensions indicated are in millimeters.

Experimental

The experimental data used for model validation were taken on a GEC reference cell modified for inductively coupled plasma operation. A schematic of the cell is shown in Fig. 3.²⁶ The power source was a five-turn coil at the top of the reactor, connected to a 13.56 MHz power supply. The substrate electrode (16.5 cm diam) was grounded and did not hold a wafer in these experiments. Gas was injected through a side port of the reactor at a rate of 5 to 20 sccm of pure chlorine. The experiments spanned the range from 20 to 50 mTorr pressure and 185 to 300 W of deposited RF power. Pressure was controlled by setting the pumping speed to maintain a desired pressure for a given flow rate without the plasma. Experimental details are given elsewhere.²⁸⁻³²

Results and Discussion

Spatially resolved electron temperature and density profiles predicted by MPRES for a chlorine plasma sustained in a GEC cell have been shown before.²⁰ Predicted

Table I. Chlorine chemical mechanism for Icarus simulations.

Gas-phase reactions	Reaction rate expressions (m^3/s) ^a	Frank-Condon energy (J)
1. $\text{Cl}_2 + e \rightarrow 2\text{Cl} + e$	$3.99 \times 10^{-14} \cdot T_e^{0.115} \cdot e^{(-4.43/Te)}$	0.96×10^{-19}
2. $\text{Cl}_2 + e \rightarrow \text{Cl}_2^+ + 2e$	$2.13 \times 10^{-14} \cdot T_e^{0.771} \cdot e^{(-11.7/Te)}$	
3. $\text{Cl} + e \rightarrow \text{Cl}^+ + 2e$	$2.96 \times 10^{-14} \cdot T_e^{0.554} \cdot e^{(-13.1/Te)}$	
4. $\text{Cl}_2 + e \rightarrow \text{Cl} + \text{Cl}^-$	$2.21 \times 10^{-16} \cdot T_e^{0.485} \cdot e^{(-0.174 \cdot Te)}$	5.78×10^{-19}
5. $\text{Cl}^- + e \rightarrow \text{Cl} + 2e$	$2.95 \times 10^{-14} \cdot T_e^{0.6801} \cdot e^{(-3.7994/Te)}$	
6. $\text{Cl}_2^+ + e \rightarrow 2\text{Cl}$	$9.00 \times 10^{-13} \cdot (300/Te \cdot 8.61753 \times 10^{-5})^{0.61}$	1.84×10^{-18}
7. $\text{Cl}_2^+ + \text{Cl}^- \rightarrow 3\text{Cl}$	5×10^{-14}	
8. $\text{Cl}^+ + \text{Cl}^- \rightarrow \text{Cl} + \text{Cl}$	5×10^{-14}	
Charge exchange reactions	Cross section (m^2), partitioning ^b	
9. $\text{Cl}_2^+ + \text{Cl}_2 \rightarrow \text{Cl}_2 + \text{Cl}_2^+$	$120 \times 10^{-20}, 0.75$	
10. $\text{Cl}^+ + \text{Cl} \rightarrow \text{Cl} + \text{Cl}^+$	$120 \times 10^{-20}, 0.75$	
11. $\text{Cl}^- + \text{Cl} \rightarrow \text{Cl} + \text{Cl}^-$	$120 \times 10^{-20}, 0.75$	
Surface reactions		
$2\text{Cl} \rightarrow \text{Cl}_2$	0.1, reaction probability	

^a Rate expressions were generated from cross sections assuming a Maxwellian electron energy distribution function. Explanation of this procedure is given in Ref. 25.

^b Charge exchange reactions were computed using collisional cross sections, instead of rate constants. The event was partitioned between a charge exchange or an elastic interaction.

profiles agreed with the measurements of Miller *et al.*²⁶ The predicted electron density reached a maximum of about $1.6 \times 10^{17}/\text{m}^3$ at the center of the discharge. The maximum predicted electron temperature of 2.6 eV occurred close to the coils, against the upper plate. Predictions of T_e were consistently below measured values. Underprediction of the electron temperature may be associated with the assumption of a Maxwellian electron energy distribution. A Maxwellian distribution has a long tail of high energy electrons, and hence a smaller T_e is predicted for a given ionization rate, which is determined by the rate of ion losses to the wall. Further comparisons with data taken in both chlorine and argon plasmas showed good correspondence between simulation and experiment.²¹ The overall agreement between predictions and experimental measurements provides a degree of confidence in the electron impact reaction rates and fields that are being imported in Icarus.

Icarus simulation results, mixed with experimental data comparisons, are presented in Fig. 4-11. Figure 4 shows predictions of the spatial profiles of Cl and Cl₂ at 185 W and 20 mTorr. Cl₂ is highly dissociated especially at the center of the reactor. The Cl mole fraction ranged from 0.85 at the center to 0.002 at the outer radius of the reactor. This represents a substantial radial gradient in the Cl number density. Wall recombination of Cl and enhanced Cl₂ dissociation around the reactor center contribute to this gradient. The predicted gradients were affected by the probability used for Cl atom wall recombination. The value of 0.1 used in this study is consistent with that found by comparing chlorine plasma data to a 0-D model.²⁷ To evaluate the influence of the Cl wall recombination probability, a series of Icarus simulations were performed with recombination probabilities ranging from 0.01 to 0.1. The predicted radial trends in neutral number densities remained fairly unchanged, although the number densities changed by a factor of two in some instances. More experimental work is needed to determine the wall recombination coefficient with certainty; however, trends in Cl density as a function of pressure and power can be predicted even without a detailed understanding of the wall chemistry.

Two-photon laser induced fluorescence (LIF) experiments of relative Cl density in the center of the GEC reactor explored trends with power and pressure.²⁸ Experimental measurements detected no change (to within 15%) in Cl density over a power range of 150 to 400 W. Simula-

tions predicted the Cl number density at the center of the discharge to remain fairly flat as a function of power, increasing from 2.3×10^{20} to $2.7 \times 10^{20}/\text{m}^3$ for a power increase from 185 to 300 W at 20 mTorr. Icarus simulations also predicted an increase in Cl density at the center of the reactor from 2.3×10^{20} to $3.7 \times 10^{20}/\text{m}^3$ when the pressure was increased from 20 to 50 mTorr. However, the mole fraction of Cl in the center of the discharge decreased with increasing pressure. In fair agreement with the simulation, the LIF experiments detected a twofold increase in Cl density at the center of the reactor for a pressure increase from 10 to 50 mTorr. (Only the normalized LIF intensity was given in Ref. 28.)

The spatial profiles of Cl⁺ and Cl₂⁺ number densities were found to be substantially different from those of the negative ion, Cl⁻, density as seen in Fig. 5. Positive ions reach their peak number density near the upper wall of the reactor. The radial profile of Cl⁺ is predicted to have a slight off-axis peak for axial locations near the coil (Fig. 6). LIF measurements of the radial profiles of the metastable Cl⁺ ions were taken at several different heights in the reactor and are also shown in Fig. 6.²⁹ Only the normalized LIF intensity was given. The measured Cl⁺ metastable ion density decreases by approximately 50% in going from 2.7 to 1.7 cm above the lower electrode. A similar drop is also measured from 1.7 to 0.7 cm above the lower electrode. The simulation predicts similar changes in Cl⁺ (ground state) number density with height above the wafer.

A comparison of the predicted radial profile of Cl⁻ density to laser photodetachment measurements, taken at the central plane of a 300 W, 20 mTorr discharge is shown in Fig. 7.³⁰ The measurements indicate a fairly flat Cl⁻ density profile with a slight increase near $r = 0.055$ m. The absolute number density of Cl⁻ ranged from 3.2×10^{17} to $4.0 \times 10^{17}/\text{m}^3$. The electrostatic fields tend to move Cl⁻ toward the center of the discharge. However Cl⁻ is formed with a significant translational energy (Table I) allowing some Cl⁻ to move opposite the field. Also, Cl⁻ is formed primarily away from the reactor center since the Cl₂ density is lowest at the center. These factors contribute to form a fairly flat Cl⁻ radial density profile. The uncertainty involved in measuring the absolute Cl⁻ density is approximately a factor of 2. However, the relative Cl⁻ density is accurate to $\pm 15\%$.³⁰ The simulation does capture the observed (rather flat) negative ion density profiles up to a radius of $r = 0.045$ cm in Fig. 7. Beyond this radial location

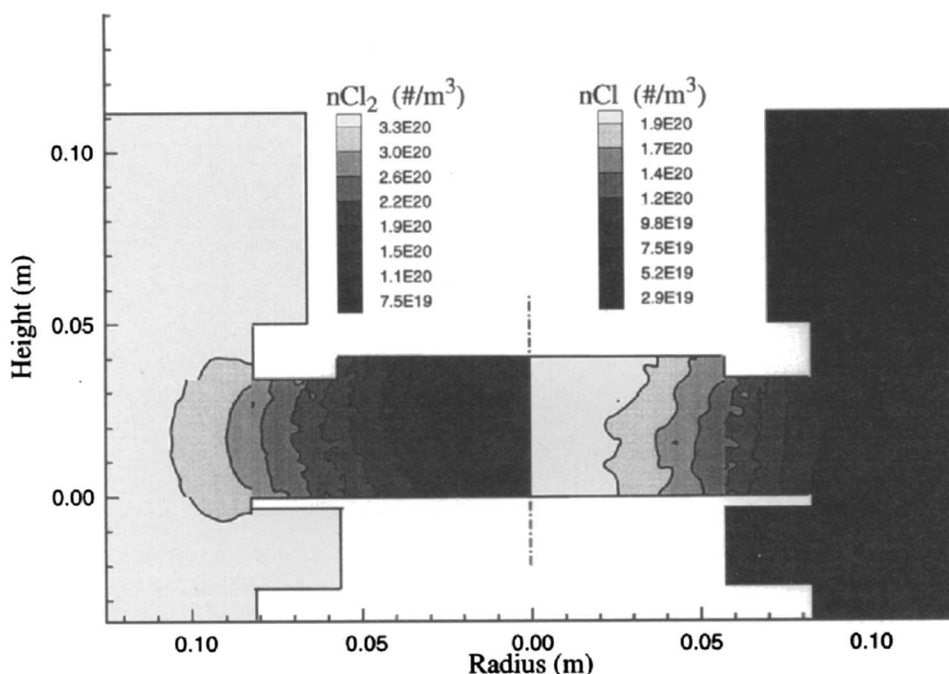
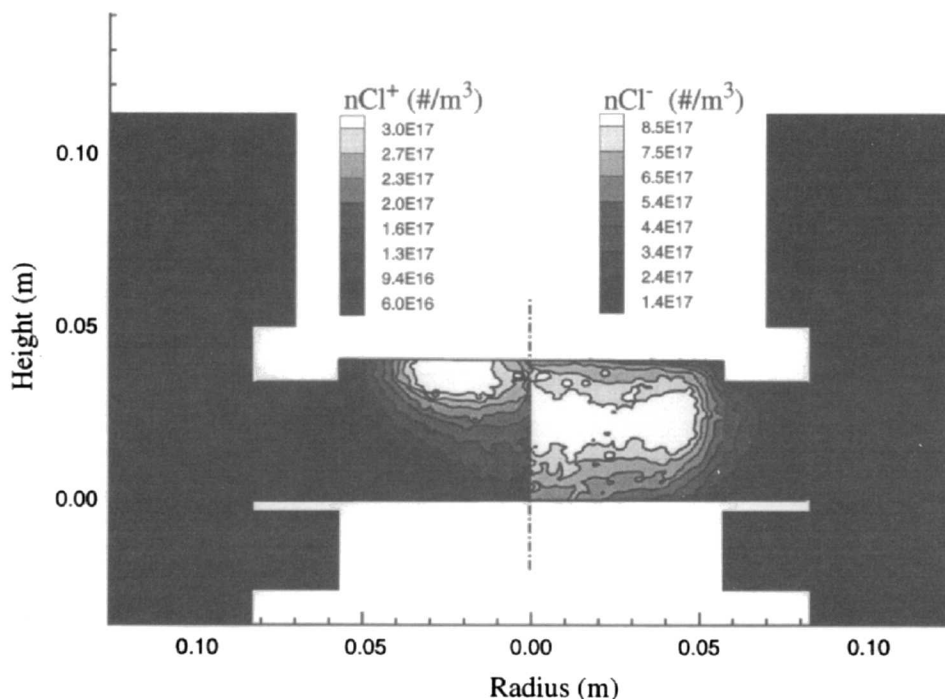


Fig. 4. Predictions of molecular chlorine (left) and atomic chlorine (right) density distributions for 185 W and 20 mTorr.

Fig. 5. Predictions of Cl^+ (left) and Cl^- (right) density distributions for 185 W and 20 mTorr.



the simulation predicts a drop in the negative ion density, in disagreement with the remaining experimental data point. The simulation results can be explained by the fact that the electrostatic fields increase with radius and at some point they become strong enough to confine the negative ions within the plasma. The origin of the apparent discrepancy with the measurements is not known at this time. It is believed, however, that the measured negative ion density has to drop when one moves further out in radius, since the plasma is fairly well confined to a radius of 0.08 m, under these conditions. Unfortunately the data does not extend far enough out in radius to test this assertion.³⁰

The flux and energy distribution of species bombarding the wafer are of critical importance since such quantities determine the etch rate, anisotropy, and selectivity, as well as the radial uniformity of these figures of merit. Predictions of the radial profiles of the flux of Cl , Cl_2 , Cl^+ , and Cl_2^+ incident on the lower electrode surface at 185 W and 20 mTorr are shown in Fig. 8. As mentioned previously, Cl^- is repelled from the potential well at the surface and does not reach the electrode. The Cl flux is decreasing with

increasing radius; the opposite trend is predicted for Cl_2 . The decrease in Cl with increasing radius is due to a decrease in n_e responsible for dissociation reactions (reactions 1 and 4, in Table I), and the wall recombination which consumes Cl to generate Cl_2 . The decrease in the Cl^+ flux with radius is associated with the drop in Cl and also n_e slowing the rate of reaction 3 (Table I). The radial profile of the Cl_2^+ flux shows a broad maximum with radius since the Cl_2 density increases, while n_e decreases with radius. However, the flux of Cl_2^+ to the surface is predicted to be much smaller than that of Cl^+ . Mass spectrometry data, taken from a pinhole in the center of the lower electrode indicated that the Cl_2^+ flux is approximately one to two orders of magnitude less than that of Cl^+ at 200 W and 20 mTorr.³¹ The slight dip in the ion fluxes along the line of symmetry is an artifact of poor statistics due to the small DSMC cell volumes at the center of the reactor. Based on the radial flux distributions shown in Fig. 8, the etch rate of polysilicon, for example, is expected to be maximum at the wafer center.

Knowledge of the angular and energy distribution functions of the species bombarding the wafer surface is also required to accurately predict etch profile evolution. Figure 9 displays the predicted angular distribution of Cl

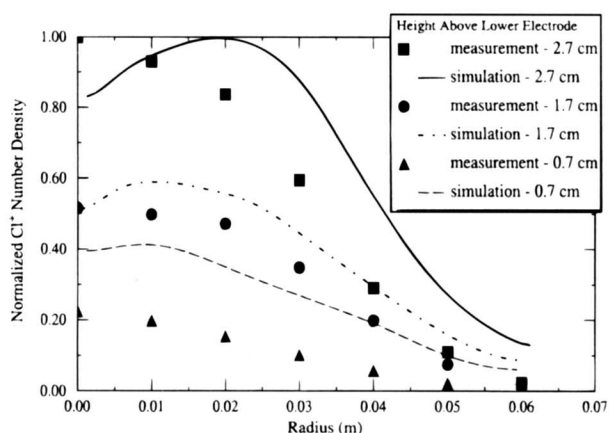


Fig. 6. Comparison of LIF measurements of Cl^+ metastable ion density radial profiles and predictions of Cl^+ ion density distributions for 185 W and 20 mTorr. LIF measurements were taken at three different heights above the lower electrode; 0.007, 0.017, and 0.027 m.

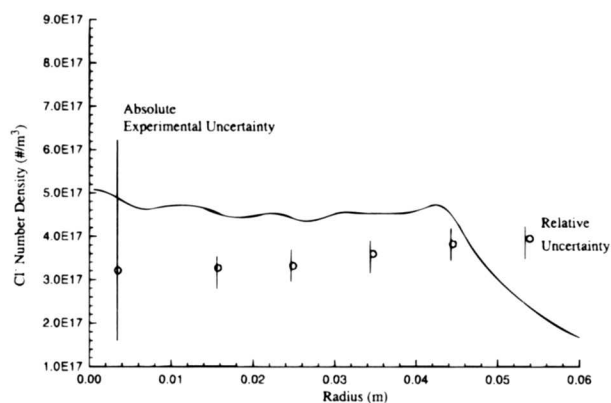


Fig. 7. Comparison of radial photodetachment measurements (circles) and prediction of Cl^- density distribution (solid line) at 300 W and 20 mTorr. Data and simulations are at a height of 0.015 m above the lower electrode.

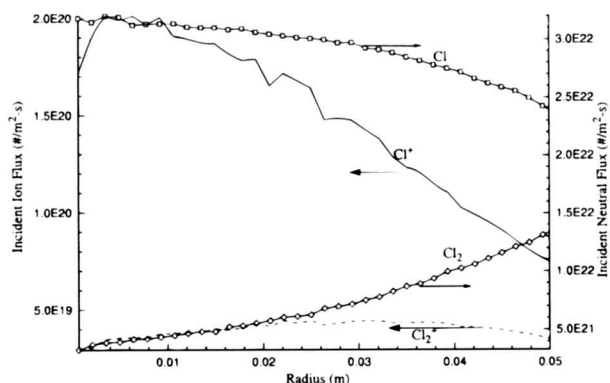


Fig. 8. Predictions of flux (1/m²-s) distributions of Cl, Cl₂, Cl⁺, and Cl₂⁺ incident on the lower electrode for 185 W and 20 mTorr. The slight dip in ion flux along the center line ($r = 0.0$) is an artifact of poor statistics due to the decreasing cell volume in the center of the reactor.

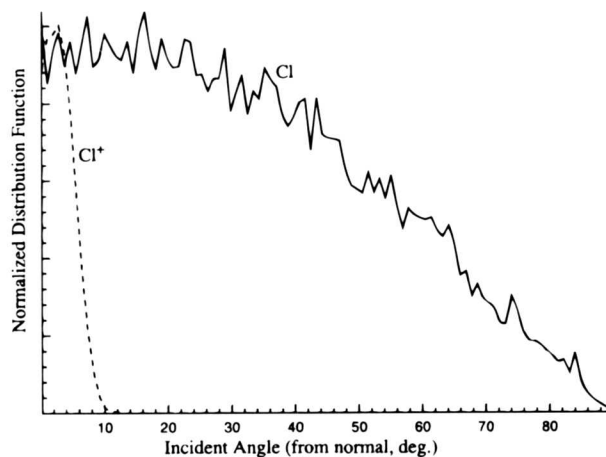


Fig. 9. Predictions of the angular distribution function of Cl (solid line) and Cl⁺ (dashed line) incident on the lower electrode at a radius of 0.03 m for 185 W, 20 mTorr.

and Cl⁺ incident on the lower electrode at $r = 0.03$ m for 185 W and 20 mTorr. As expected, the Cl radicals are much more thermalized than the ions, although the radical distribution does not correspond to a perfect Maxwellian. Deviations from a perfect Maxwellian distribution are

associated with Frank-Condon effects realized when Cl is created via reactions 1 and 6, for example (Table I). Deviations from thermal equilibrium were also predicted in the neutral species temperatures; an average tempera-

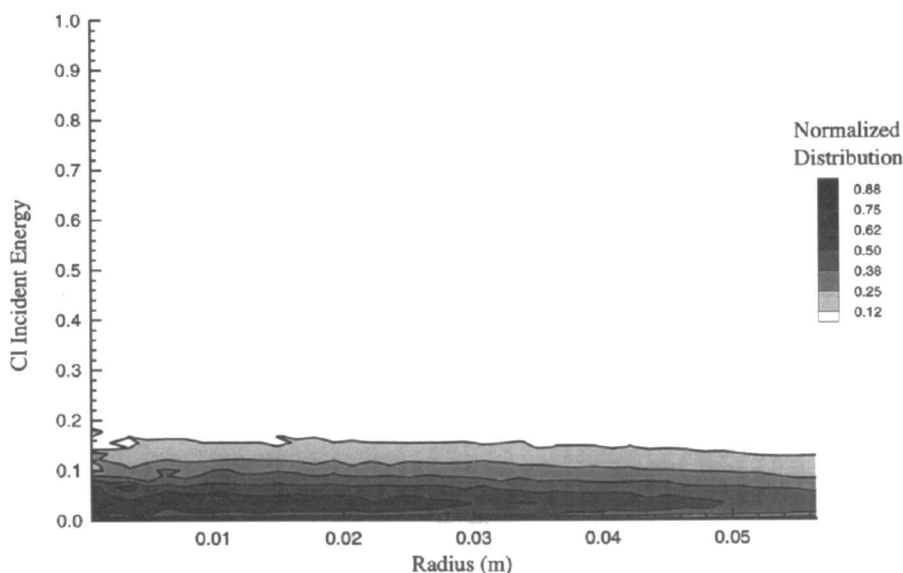
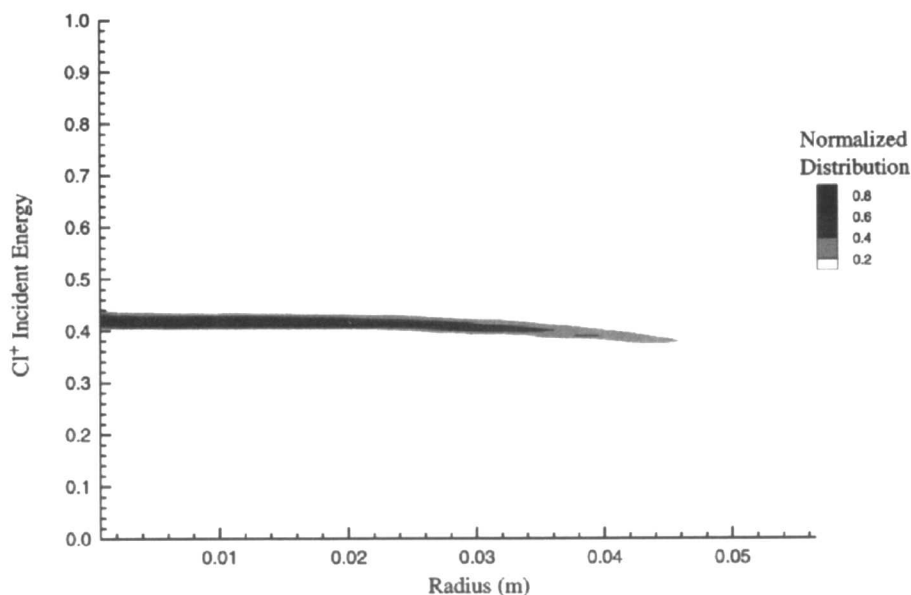


Fig. 10. 2-D representation of energy distribution functions (eV) incident on the lower electrode for 185 W and 20 mTorr for (a, top) Cl⁺, and (b, bottom) Cl.

ture of 515 K was predicted for Cl at the center of a 185 W discharge, while the Cl₂ temperature was slightly lower at 492 K. Cl⁺ is predicted to hit the surface within several degrees of normal.^{31,32} Similar angular distributions were predicted for Cl₂⁺. The radical and ion angular distribution functions were predicted to undergo minor alterations in peak width and shape as a function of radius along the bottom electrode.

Figures 10a and b show the predicted energy distribution functions for Cl⁺ and Cl, respectively, plotted against radius for 185 W and 20 mTorr. A very narrow distribution is predicted for the ions with the maximum energy of 12.5 eV at $r = 0.0$ m, decreasing to 12.0 eV at $r = 0.045$ m. The Cl distribution function is predicted to have a more pronounced peak for $r < 0.03$ m, where the Cl concentration is highest. A tail of neutrals with high energy is created from exothermic reactions (reactions 1, 4, and 6) and charge exchange reactions (reactions 9 and 10 in Table I).

Figure 11 shows the predicted incident Cl⁺ energy distribution function compared to measurements taken by Woodworth *et al.*³¹ The experimental peak of the distribution function is at 11 eV, at the center of the electrode for 200 W and 20 mTorr. This is slightly lower than the predicted value. The energy measurements were sensitive to the wall temperature and the peak energy shifted by 1 to 2 eV as the system heated up. This can easily account for differences between measurements and predictions. Collisions in the presheath are likely to be responsible for the slightly wider distribution noted in the experimental data. The bulk plasma/sheath approximation made in the simulation negates this effect. For HDP systems in which an RF bias is applied to the lower electrode, bimodal distributions are often observed in the ion energy distribution functions. Such distributions can be predicted by the sheath model.²³

Summary

Two-dimensional DSMC-fluid hybrid simulations were performed for an inductively coupled plasma in chlorine, sustained in a Gaseous Electronics Conference reference cell. Simulation conditions ranged from 20 to 50 mTorr pressure and 185 to 300 W plasma power.

Experimental data available for comparison with the simulation results included radial profiles of n_e , T_e , Cl⁻ density, Cl⁺ density, as well as trends of Cl radical density with power and pressure. The DSMC-fluid hybrid predictions agreed fairly well with the data within experimental accuracy. Limited data on ion fluxes and ion energy distributions were also in agreement with the simulation results. Particle simulations such as DSMC are powerful tools for predicting the behavior of rarefied (low gas pres-

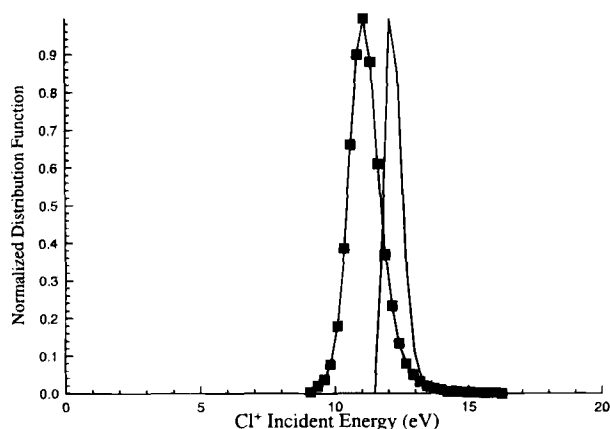


Fig. 11. Comparison of incident Cl⁺ energy distribution function predicted by Icarus (line without points) and ion energy analyzer data (line with points). Predictions are for 185 W, 20 mTorr at a radius of $r = 0.03$ m. Data was taken at $r = 0.0$ m, 200 W, and 20 mTorr.

sure) plasma systems, especially for predicting the angular and energy distributions of etchant species bombarding the wafer.

A limiting factor in using Icarus, or any plasma model, to predict plasma reactor performance for industrially relevant systems is lack of fundamental information on gas-phase chemistry and especially on surface reaction mechanisms. This is particularly true for realistic systems employing gas mixtures and where etching and deposition reactions occur simultaneously. However, simulation tools must first be validated against "cleaner" (but still relevant) chemistries such as the chlorine chemistry used here.

Acknowledgments

We thank Dr. Wahid Hermina and Dr. Merle Riley of Sandia National Laboratories, Albuquerque, for many helpful discussions throughout this work. The technical assistance of Tom Hamilton is gratefully acknowledged. This work was funded by a Sandia-SEMATECH CRADA and was performed at Sandia National Laboratories which is operated for the DOE under Contract DE-AC04-76DP00789. Work at the University of Houston was supported in part by a National Science Foundation Grant (CTS-9216023).

Manuscript submitted Aug. 5, 1996; revised manuscript received April 7, 1997.

Sandia National Laboratories assisted in meeting the publication costs of this article.

REFERENCES

1. J. Hopwood, *Plasma Sources Sci. Technol.*, **1**, 109 (1992).
2. J. H. Keller, J. C. Foster, and M. S. Barnes, *J. Vac. Sci. Technol.*, **A11**, 2487 (1993).
3. E. Meeks and J. W. Shon, *IEEE Trans. Plasma Sci.*, **23**, 539 (1995). See also entire collection of papers in that issue of *IEEE Trans. Plasma Sci.*
4. J. D. Bukowski, D. B. Graves, and P. Vitello, *J. Appl. Phys.*, **80**, 2614 (1996).
5. D. Lymberopoulos and D. J. Economou, *IEEE Trans. Plasma Sci.*, **23**, 573 (1995).
6. M. J. Kushner, W. Z. Collision, M. J. Grapperhaus, J. P. Holland, and M. S. Barnes, *J. Appl. Phys.*, **80**, 1337 (1996).
7. Y. Yang and H. Wu, *ibid.*, **80**, 3699 (1996).
8. U. Kortshagen, I. Pukropski, and L. D. Tsengin, *Phys. Rev. E*, **51**, 6063 (1995).
9. M. Surendra, *Plasma Sources Sci. Technol.*, **4**, 56 (1995).
10. G. A. Bird, *Molecular Gas Dynamics and the Direct Simulation of Gas Flows*, Oxford Science Publications, Oxford (1994).
11. W. L. Hermina, in *Proceedings of 15th International Symposium on Rarefied Gas Dynamics*, Vol. 1, 451 (1986).
12. T. J. Bartel and S. J. Plimpton, Paper AIAA 92-280, 27th AIAA Thermophysics Conference, Nashville, TN (1992).
13. P. K. Shuffelbotham, T. J. Bartel, and B. Berney, *J. Vac. Sci. Technol.*, **13**, 1862 (1995).
14. A. Kersch, W. Morokoff, and C. Werner, *J. Appl. Phys.*, **75**, 2278 (1994).
15. A. M. Meyers, J. R. Doyle, and D. N. Ruzic, *ibid.*, **62**, 3064 (1992).
16. D. G. Coronell and K. F. Jensen, *This Journal*, **139**, 2264 (1992).
17. M. D. Kilgore, H. M. Wu, and D. B. Graves, *J. Vac. Sci. Technol.*, **12**, 494 (1994).
18. V. Serikov and K. Nanbu, *J. Vac. Sci. Technol.*, **A14**, 3108 (1996).
19. D. Economou, T. Bartel, R. Wise, and D. Lymberopoulos, *IEEE Trans. Plasma Sci.*, **23**, 581 (1995).
20. R. S. Wise, D. P. Lymberopoulos, and D. J. Economou, *Appl. Phys. Lett.*, **68**, 2499 (1996).
21. D. Economou, R. Wise, and D. Lymberopoulos, in *Proceedings of the 11th International Symposium on Plasma Processing*, G. S. Mathad and M. Meyyappan, Editors, PV 96-12, p. 11, The Electrochemical Society Proceedings Series, Pennington, NJ (1996).
22. E. F. Jaeger and L. Berry, *Phys. Plasmas*, **2**, 2597 (1995).

23. M. Riley, *Unified Model of the RF Plasma Sheath*, Sandia National Laboratories Report, SAND95-0775 (1995).
24. M. A. Lieberman and A. J. Lichtenberg, *Principles of Plasma Discharges and Materials Processing*, John Wiley & Sons, New York (1994).
25. N. L. Bassett and D. Economou, *J. Appl. Phys.*, **75**, 1931 (1994).
26. P. Miller, G. Hebner, K. Greenberg, P. Pochan, and B. Aragon, *J. Res. Natl. Inst. Stand. Technol.*, **100**, 427 (1995).
27. E. Meeks and J. Shon, *IEEE Trans. Plasma Sci.*, **13**, 2884 (1995).
28. G. Hebner, *J. Appl. Phys.*, **81**, 578 (1997).
29. G. Hebner, C. B. Fledderman, and P. A. Miller, *J. Vac. Sci. Technol.*, Submitted.
30. G. Hebner, *J. Vac. Sci. Technol.*, **A14**, 2158 (1996).
31. J. Woodworth and M. Riley, *Ion Energy and Angular Distributions in Inductively Driven RF Discharges in Chlorine*, Sandia National Laboratories Report, SAND96-0559 (1996).
32. J. R. Woodworth, M. E. Riley, D. C. Meister, B. P. Aragon, M. S. Le, and H. H. Sawin, *J. Appl. Phys.*, **80**, 1304 (1996).

X-Ray Photoelectron Spectroscopy Analyses of Oxide-Masked Polycrystalline SiGe Features Etched in a High-Density Plasma Source

C. Monget, S. Vallon,^a F. H. Bell,^b L. Vallier,^a and O. Joubert^a

France Telecom - CNET, 38243 Meylan Cedex, France

ABSTRACT

The chemical distribution of oxide-masked polycrystalline Si_{0.45}Ge_{0.55} structures etched using gas mixtures of Cl₂, HBr, and O₂ has been investigated by x-ray photoelectron spectroscopy (XPS). The 200 mm diam wafers were etched in a low-pressure, high-density plasma helicon source. The chemical constituents present on the tops, sidewalls, and bottoms of the etched features were determined by XPS. As for polysilicon, a silicon oxide-like film is formed on the sidewalls of the features when etching with HBr/Cl₂/O₂ and Cl₂/O₂ plasmas, whereas there is no germanium oxide-like formation. Using XPS, the silicon oxide-like layer was estimated to be 11 Å thick on the sidewalls of the poly Si_{0.45}Ge_{0.55} with both mixtures. The thinner oxide-like layer measured on the sidewalls of polycrystalline Si_{0.45}Ge_{0.55} (11 Å) compared to that on the sidewalls of polycrystalline Si (30 Å) demonstrates that the oxide-like layer thickness depends on the germanium concentration in the alloy. XPS also shows that by using the Cl₂/O₂ gas mixture, the germanium of the polycrystalline SiGe sidewalls spontaneously reacts with oxygen to form volatile etching species.

Introduction

Single-crystal silicon-germanium alloys have been extensively studied for device applications. Polycrystalline Si_xGe_{1-x} (referred to as poly SiGe hereafter) has recently been demonstrated to be a suitable alternative to the polycrystalline Si (poly Si) gate electrode for complementary metal oxide semiconductor (CMOS) technology.¹ The advantage of using poly SiGe as a gate material is that its work function is tunable as a function of the Ge concentration in the alloy. Furthermore, poly-Ge (a so-called midgap material) allows the use of single heavily p-doped (P⁺) polycide gates instead of the traditional P⁺/N⁺ doped material. Several studies have explored the etching of a SiGe alloy for Si/SiGe heterostructure applications.^{2,3} In particular, the anisotropic etching of SiGe structures down to 0.2 μm has been reported.⁴

Recently we investigated the patterning of oxide-masked polysilicon gates in a high-density plasma helicon source using HBr/Cl₂/O₂ gas mixtures.⁵ An etching recipe has been optimized allowing the development of 0.2 μm polysilicon gates on thin gate oxides (thickness < 4 nm). On the other hand, the recipe developed for oxide-masked poly-Si gates cannot be used to pattern bilayer poly-Si/poly SiGe gates (a strong deformation of the etching profiles has been observed).⁶ A two-step etching recipe using a Cl₂/O₂-He gas mixture has been optimized, allowing perfectly anisotropic 0.2 μm poly-Si/poly Si_{0.45}Ge_{0.55} gates to be developed.⁶

In this study we used XPS to determine the chemical distribution of silicon dioxide-masked poly Si_{0.45}Ge_{0.55} features etched in a high-density plasma helicon source using

mixtures of HBr, Cl₂, and O₂-He. XPS analyses have allowed the chemical composition of the poly Si_{0.45}Ge_{0.55} sidewalls to be determined and a better understanding of the etching mechanism to be achieved.

Experimental

The system used for these experiments is a high-vacuum cluster tool consisting of a load lock chamber, transfer chamber, reactor chamber, and XPS analysis chamber. The analysis chamber has been used in previous studies and is described in detail elsewhere.⁷ It is equipped with an x-ray photoelectron spectrometer (Fisons Surface Systems ESCALAB 220i), a single electrostatic lens flood gun (VG Model LEG 41), and a mass spectrometer (Micromass 386). The XPS system provides the possibility of analyzing 200 mm wafers. The analysis chamber is equipped with a nonmonochromatized twin anode (Al K_α, 1487 eV/Mg K_α, 1253.6 eV) and a monochromatized Al K_α x-ray source. The latter was used for all experiments performed in this study and operated in a 1000 μm spatial resolution mode, providing an x-ray spot diameter of less than 1 mm. An electron flood gun emitting low-energy electrons (0 to 80 eV) was used for charge neutralization.

The helicon source made by Lucas Labs^{8,9} has been described in more detail in previous papers.¹⁰ The etching chamber consists of a plasma generation region in which a helicon source is operated at 13.56 MHz,¹¹ and a plasma diffusion region. The plasma generation region is equipped with two solenoid magnets which are necessary to initiate the plasma, whereas two other solenoid magnets around the diffusion region maintain a high plasma density on the sample. The sample can be biased independently of the production of plasma using a 600 W maximum power supply at 13.56 MHz. The tuning of the matching network is computer controlled and performed automatically. Helium back side cooling at 10 Torr is provided to achieve a ther-

^a Present address: Siemens AG, HL PES 13, 81739, Munchen, Germany.

^b Also at LPCM-UMR 110-IMN, 44072 Nantes Cedex 03, France.